The Journal of Chemical Physics

RESEARCH ARTICLE | AUGUST 02 2023

Evaporation and scattering of neon, methane, and water from a dodecane flat liquid jet

Walt Yang ; Chin Lee ; Steven Saric ; Marvin N. Pohl ; Daniel M. Neumark

J. Chem. Phys. 159, 054704 (2023)
https://doi.org/10.1063/5.0159796

The Journal of Chemical Physics ARTICLE pubs.aip.org/aip/jcp

Evaporation and scattering of neon, methane, and water from a dodecane flat liquid jet

Cite as: J. Chem. Phys. 159, 054704 (2023); doi: 10.1063/5.0159796
Submitted: 26 May 2023 • Accepted: 17 July 2023 •
Published Online: 2 August 2023

Walt Yang,[1,2] Chin Lee,[1,2,a)] Steven Saric,[1,2] Marvin N. Pohl,[1,2,b)] and Daniel M. Neumark[1,2,c)]

AFFILIATIONS

[1] Department of Chemistry, University of California, Berkeley, California 94720, USA
[2] Chemical Sciences Division, Lawrence Berkeley National Laboratory, Berkeley, California 94720, USA

[a)] **Present address:** Chin Lee – Gas Phase Chemical Physics, Sandia National Laboratories, Livermore, CA 94550, USA.
[b)] **Present address:** Marvin N. Pohl – BASF Coatings GmbH, Glasuritstraβe 1., 48165 Münster-Hiltrup, Germany.
[c)] **Author to whom correspondence should be addressed:** dneumark@berkeley.edu

ABSTRACT

The evaporation and scattering of Ne, CD_4, and D_2O from a dodecane flat liquid jet are investigated in a molecular beam apparatus. The experiment yields translational energy distributions as a function of scattering angle by means of a rotatable mass spectrometer. In the evaporation experiments, one observes a Maxwell–Boltzmann distribution with a $\cos\theta$ angular distribution superimposed on a weak, isotropic background. The scattering experiments show contributions from impulsive scattering and thermal desorption. At select incident angles for the three systems, angular distributions show super-specular scattering for the impulsive scattering channel, an effect attributed to anisotropic momentum transfer to the liquid surface. The impulsive scattering channel is analyzed with a soft-sphere model to explore energy transfer between the scatterer and liquid as a function of deflection angle. Compared to Ne scattering, the polyatomic gases exhibit more thermal desorption and, in the impulsive scattering channel, a higher degree of internal excitation.

I. INTRODUCTION

The gas–liquid interface is a chemical environment omnipresent in nature. It plays a key role in the physiology of the air–lung interface[1] and in industrial processes such as air–fuel mixing in internal combustion engines.[2] It is also instrumental in atmospheric chemistry and environmental science through acid rain formation,[3–5] tropospheric aerosol surface chemistry,[6] and the uptake of anthropogenically generated carbon dioxide at the ocean–air interface.[7] Previous studies have shown that interfacial chemistry can substantially differ from the interactions that take place in bulk liquids.[8–13] For example, enhanced surface chemical reaction rates have been reported compared to bulk reaction rates in studies of thin films and microdroplets,[14–16] and surface-specific spectroscopic properties along with interfacial structural information have been gathered through sum frequency generation techniques.[17–19]

Molecular beam scattering has proved to be a complementary and powerful method for studying interfacial chemistry. This method was originally developed to study single collision dynamics between gas phase molecules[20–22] and scattering from solid surfaces.[23–28] More recently, Nathanson and co-workers have pioneered experiments in which molecular beams scatter from liquid surfaces, uncovering unprecedented mechanistic detail behind gas–liquid interfacial interactions.[29,30] Here, we report experiments on the evaporation and molecular beam scattering of CD_4 and D_2O from a flat liquid jet of dodecane. We compare our results to a revisit of a recent study on Ne evaporation and scattering from dodecane in our laboratory[31] and to earlier experiments by the groups of Nathanson and Minton on scattering from squalane.[32,33]

Previous work on molecular beam scattering from both liquid and solid surfaces has revealed two limiting mechanisms at the interface, impulsive scattering (IS) and thermal desorption (TD), associated with fast and slow velocity distributions, respectively.[29,34] In the IS limit, incident gas molecules recoil from the surface elastically or only lose a fraction of their initial energy. On the other hand, TD represents molecules with residence times long enough at the liquid surface to experience a two-step surface-trapping mechanism comprising thermalization and subsequent desorption. In the IS channel, gas scattering partners are detected preferentially at

outgoing angles highly dependent on initial energy and impact angle, whereas TD ideally yields a $\cos\theta$ angular distribution with respect to the surface normal.[24,35] This simple dichotomy provides a limiting rather than all-encompassing explanation for scattering at the gas–liquid interface; however, it is still a useful framework for the interpretation of our results, and we use it as such throughout this work.

In order to perform molecular beam scattering experiments targeted at the gas–liquid interface, the sample must possess a clean surface and be compatible with a vacuum environment. Originally, a "wetted wheel" approach[36,37] was used to study low vapor pressure systems ($<10^{-3}$ Torr) with success.[33,38–41] The development of vacuum-compatible, micrometer-thin cylindrical jets by Faubel and co-workers[42,43] enabled scattering experiments to be carried out on higher vapor pressure, more volatile liquids, such as dodecane,[44] surfactant-coated glycerol,[45,46] and salty water.[47,48] Although scattering experiments based on these methods have elucidated interfacial interactions and reactivity, the wetted wheel is unsuitable for high vapor pressure liquids in a vacuum chamber, while cylindrical jets present a very small scattering target and do not allow for well-defined scattering angles.[30]

These considerations motivated a recent study in our laboratory[31] in which we scattered a beam of Ne atoms from a flat liquid jet of dodecane generated by a microfluidic chip as the liquid source.[49] The flat liquid jet offers significant advantages in such experiments as its dimensions are more commensurate with those of a typical molecular beam (~1 mm), yielding a considerably improved signal-to-noise ratio compared to scattering from a cylindrical jet. Moreover, the flat jet presents a well-defined surface normal for the measurement of angular distributions. We measured the angular and translational energy distributions for Ne evaporation and Ne scattering from dodecane, demonstrating the feasibility of probing interactions at the gas–liquid interface for a liquid whose vapor pressure ($P_{vap} = 1.5 \times 10^{-2}$ Torr at 275 K) is too high for a wetted wheel experiment. We also measured IS/TD ratios for various scattering angles and analyzed the IS pathway to determine energy transfer at the interface as a function of deflection angle.

A natural extension of this work is to scatter molecules with the same mass as Ne from a dodecane flat jet. Nathanson previously investigated the scattering of Ne, methane, and deuterated water from a squalane ($P_{vap} = 10^{-7}$ Torr at 295 K) wetted wheel,[32] where it was found that Ne scattering resulted in a higher IS/TD ratio than CH_4 and D_2O scattering. Energy transfer at the gas–liquid interface was higher for both polyatomic molecules than for Ne. However, this study was performed at a fixed deflection angle, limiting a key parameter in characterizing interfacial interactions. The scattering of Ne from squalane was also investigated theoretically by Hase and co-workers by means of classical trajectory calculations.[50]

Here, we examine the scattering of CD_4 and D_2O from a dodecane flat jet to explore the effects of additional degrees of freedom in a molecular scatterer. Improvements to the operation of the mass spectrometer since our first paper led us to re-investigate Ne scattering as well. CD_4 is larger and more polarizable than Ne, while D_2O possesses a nonzero dipole moment. In addition, the solubilities of the three scatterers in hydrocarbons differ, as summarized in Table I.

As before, we carry out evaporation and scattering experiments to characterize the IS and TD channels through the measurement of angular and translational energy distributions. For certain incident angles, the maximum intensity of the IS channel occurs at non-specular outgoing angles due to anisotropic momentum transfer to the surface. We find considerably more TD with the molecular scatterers than for Ne, although the angle-dependent trends for IS vs TD are similar. Additionally, fitting the IS channel to a kinematic model for surface scattering as a function of deflection angle shows more loss of incident translational energy for the polyatomic gas scatterers that is attributed to the rotational excitation of these species from collisions with the liquid surface.

II. EXPERIMENTAL METHODS

Experiments are carried out on a crossed molecular beam instrument[47,48] adapted for gas–liquid scattering, as described in detail previously.[31,53,54] Three regions, evacuated by turbomolecular pumps, comprise the total apparatus—a source chamber where the molecular beam is generated, a collision chamber where the beam interacts with the liquid jet, and a triply differentially pumped rotatable detector chamber housed within the collision chamber that comprises an electron impact ionizer, a quadrupole mass filter, and an ion detection assembly. Furthermore, details regarding the modifications made to render this apparatus appropriate for the study

TABLE I. Properties of select gas scattering partners.

	Ne	CD_4[a]	D_2O
Radius (Å)[b]	1.5	2.0	~1.4
Polarizability (Å^3)[b]	0.4	2.6	1.3
Dipole moment (D)[b]	0	0	1.8
Solubility in dodecane K_H (x_{soln}/P_{vap})[c]	3.48×10^{-4}	5.45×10^{-3}	1.95×10^{-2}[d]
Free energy of solvation ΔG°_{solv} (kJ mol^{-1})[e]	18.1	11.8	8.94

[a]Values reported for CH_4.
[b]Taken from Ref. 32.
[c]Taken from Refs. 51 and 52. Values reported at a partial pressure $P = 1$ atm and a temperature $T = 298.15$ K.
[d]Value reported for H_2O.
[e]The free energy of solvation is given by $\Delta G^\circ_{solv} = -RT \ln K_H$.

of gas–liquid scattering can be found in our previous work.[31] A schematic of the scattering setup is shown in Fig. 1.

In the source chamber, a pulsed molecular beam is generated using a piezoelectric valve (MassSpecpecD BV, Enschede).[55,56] The neon molecular beam is prepared by seeding Ne (99.99% purity) in helium at a 1:9 ratio. The methane molecular beam is prepared by seeding 0.75% CD_4 (99% purity, 99% D, Sigma–Aldrich) in helium. Stagnation conditions for both the Ne and CD_4 molecular beams are typically 290 K and 3000 Torr, resulting in a supersonic expansion of the gas mixture through the 500 μm valve orifice. The water molecular beam is prepared by bubbling helium gas through a glass reservoir containing D_2O (99% D, Sigma–Aldrich) held at 4 °C in a single pass. Stagnation conditions are typically 290 K and 1100 Torr, optimized toward minimizing the fraction of water dimers present in the beam. In order to quantify dimer formation, we measured the intensity of D_2O^+ and $(D_2O)D^+$, the primary ion fragments of the deuterated water monomer and dimer subject to electron ionization.[57–59] We found that the $(D_2O)D^+$ to D_2O^+ ratio was consistently at or below 5% under these conditions. During water evaporation experiments, a dimer ratio of 6% was present. No multimers beyond dimers for D_2O and no dimers for CD_4 were detected.

To investigate gas–liquid interactions, a liquid jet is generated in the collision chamber by a microfluidic chip.[49] The chip can be configured toward cylindrical or flat jet operation as described previously; however, we exclusively present results from the flat jet mode in this work. The liquid is transported to the jet nozzle at a flow rate of 3.5 ml min^{-1}. This results in a flow velocity of 10 ms^{-1}, corresponding to a detector viewing time of ~0.5 ms in evaporation and scattering experiments (~5 mm at the interaction region with the detector gate valve opened to a 3 × 3 mm^2 aperture). The typical dimensions of the first flat jet sheet are 1.5 × 4.5 mm^2 (W × H) with a thickness estimated to be ~1.5 μm at its center.[60]

The solvent is cooled prior to arriving at the jet nozzle, and the temperature of the liquid jet is recorded using a thermocouple attached to the stainless-steel chip holder. We assume that this

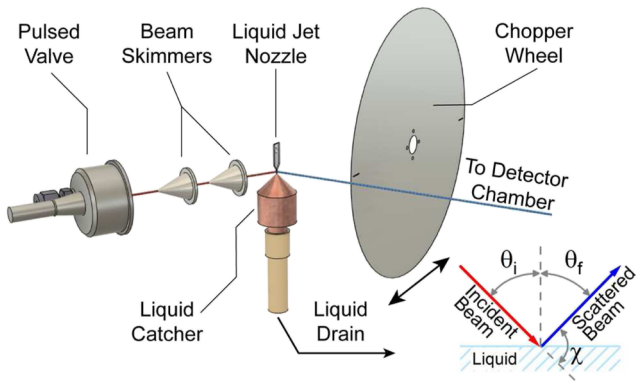

FIG. 1. Schematic diagram of the scattering setup. All components are situated inside the collision chamber (not shown). Lines indicate the molecular beam (red trace) striking the flat liquid jet surface and scattering from it (blue trace). The chopper wheel can be translated perpendicular to the detector axis (indicated by the heavy double-sided arrow). The inset schematic defines the incident angle θ_i, detector angle θ_f, and deflection angle $\chi = 180° - (\theta_i + \theta_f)$.

T_{holder} is equal to the temperature of the liquid at the chip outlet. The true liquid temperature T_{liq} is defined as the jet temperature at the detector axis. The temperature difference $T_{holder} - T_{liq}$ is estimated to be less than 0.5 °C owing to the high isobaric heat capacity and low vapor pressure of dodecane.[61,62] In the evaporation experiments, T_{liq} = 273 and 274 K for dodecane doped with CD_4 and D_2O, respectively, and T_{liq} = 269 K for all scattering experiments.

The velocities of the molecular beams are characterized by time-of-flight (TOF) measurements using a rotating chopper wheel spinning at 200 Hz. This disk contains two slits (16 μs opening time) to temporally "chop" the most intense part of the beam. For evaporation experiments, the chopper is present along the detector axis, and its position is used to set time zero for the TOF spectra. During scattering experiments, the wheel is removed, and time zero is defined as when the most intense part of the molecular beam reaches the interaction region. For Ne, CD_4, and D_2O, the velocities are 1562 ± 165, 1732 ± 185, and 1791 ± 347 ms^{-1} (FWHM), with mean translational energies of 23.7, 29.3, and 33.4 kJ mol^{-1}, respectively.

In the evaporation experiments, no molecular beam is present, and the liquid surface is positioned such that the surface normal is perpendicular to the molecular beam axis. The resulting detector angles θ_f then range from 0° to 90° with respect to the surface normal. To prepare the sample, either CD_4 or D_2O is dissolved in dodecane (n-$C_{12}H_{26}$, TCI America No. D0968). For CD_4, this is achieved by vacuum-degassing the liquid. The liquid reservoir was simultaneously sonicated and pumped with a mechanical pump for 10 min, followed by bubbling the 0.75% CD_4/He mixture until the reservoir is pressurized slightly higher than atmospheric pressure (~850 Torr). This cycle was performed five times. Prior to preparing the D_2O sample, the dodecane reservoir was vacuum degassed with pure He in an analogous manner as described earlier. Then, ~1 ml of D_2O was added to ~500 ml of dodecane and stirred overnight. After stirring, the sample was vacuum degassed for only one cycle. Care was taken to ensure that the remaining pure D_2O after stirring was not incorporated into the liquid jet.

In the scattering experiments, pure dodecane was used after vacuum-degassing with pure He. The incident angle θ_i, scattering angle θ_f, and deflection angle $\chi = 180° - (\theta_i + \theta_f)$ are defined in Fig. 1. The incident angle θ_i, set by rotation of the flat jet, is chosen to be either 45°, 60°, or 80°. Outgoing angles θ_f are then confined to between $90° - \theta_i$ and 90° due to the geometry of the scattering apparatus. This results in a deflection angle χ with minimum values of 45°, 30°, and 20° for the above-mentioned three values of θ_i, respectively. Each incident angle shares the same maximum deflection angle of 90°. Since the chopper wheel is removed in the scattering experiments, the temporal resolution of the measurement is limited by the duration of the pulsed beam. For Ne and CD_4, the valve opening time is set to 15 μs, while it is set to 30 μs for D_2O. This results in temporal widths of 28, 26, and 43 μs measured at the detector, respectively (see Sec. III). Background correction is performed by subtracting "beam-off" from "beam-on" data.

To account for long-term signal instabilities and reduce systematic error in the evaporation experiments, angular distributions from the flat liquid jet are measured in a back-and-forth manner from integrated TOF spectra collected at θ_f ranging from 0° to 90°.

Setting the 0° TOF spectrum as our reference, all other signal intensities are calibrated as required. For the scattering experiments, the integrated TOF spectra collected at θ_i = 45°, 60°, and 80° are calibrated to the corresponding θ_f = 45°, 90°, and 80° TOF spectra, respectively. Acquisition times at each angle are typically 5–10 min, and all data are collected with 80 eV electron kinetic energy from the ionizer.

III. RESULTS AND ANALYSIS

A. Evaporation

Evaporation studies of CD_4- and D_2O-doped dodecane solutions isolate the TD pathway. TOF spectra of CD_4 and D_2O evaporating from flat jets of their doped dodecane counterparts are shown in Fig. 2. The evaporation of CD_4 is shown in Fig. 2(a) for detector angles θ_f of 0°, 30°, 60°, and 90°. Analogous spectra for D_2O are shown in Fig. 2(b). Upon integrating the fitted TOF spectra, angular distributions are generated where total intensity is plotted as a function of θ_f in Fig. 3(a) for CD_4 and Fig. 3(b) for D_2O.

When evaporating particles are fully thermalized with the surface liquid, the product flux f can be described by a Maxwell–Boltzmann (MB) flux distribution,[63]

$$f_{MB}(v) \propto v^3 \exp\left(-\frac{mv^2}{2RT_{liq}}\right), \quad (1)$$

where v and m are the velocity and molecular mass of the evaporating molecule, and R is the universal gas constant. We find that the TOF spectrum at θ_f = 0° is well-fitted by an MB distribution at T_{liq},

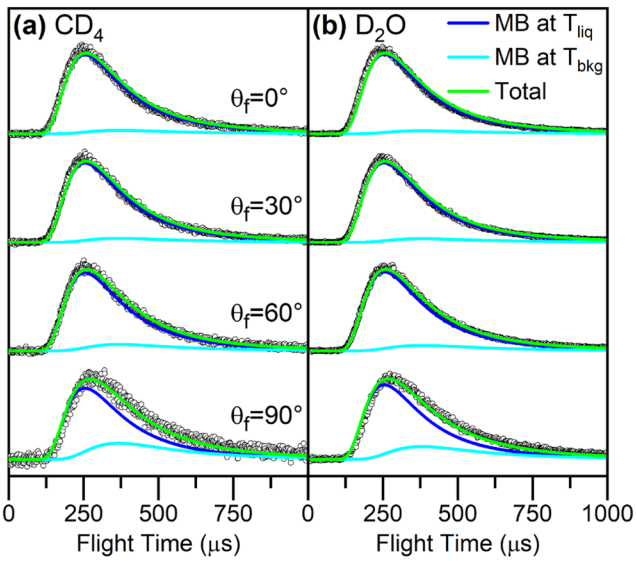

FIG. 2. Normalized evaporation TOF spectra of (a) CD_4 from a CD_4-doped liquid dodecane flat jet at 273 K and (b) D_2O from a D_2O-doped liquid dodecane flat jet at 274 K. TOF distributions are fitted with a combination of Maxwell–Boltzmann velocity distributions at the liquid temperature (blue traces) and at T_{bkg} = 131 K for CD_4 evaporation and 123 K for D_2O evaporation (light blue traces). The absolute intensity of the T_{bkg} component is kept constant for all angles. The sum of the two contributions is shown by the green traces.

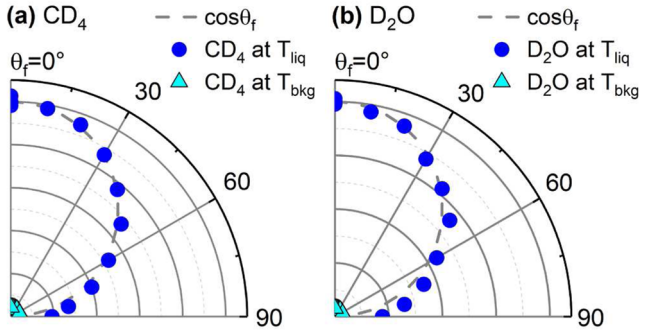

FIG. 3. Angular plots created from the integrated, non-normalized intensities of the Maxwell–Boltzmann simulations at T_{liq} and T_{bkg} (blue circles and cyan triangles, respectively) of (a) CD_4 and (b) D_2O evaporation data at various detector angles. The cosine function representing the expected angular distribution for evaporation is indicated by the dashed gray curve.

and there is a slight broadening of the temporal distribution toward longer times as θ_f increases. At θ_f = 90°, the evaporation profiles for both CD_4 and D_2O are slower and broader than at all other detector angles.

These "sub-Maxwellian" distributions at increasing θ_f were also seen in our previous study on the evaporation of Ne from Ne-doped dodecane jets, where we found that the corresponding TOF profiles could be represented by a linear combination of MB distributions, one of which captures the Ne evaporation process at T_{liq} while the other accounts for a constant cold evaporative Ne background at T_{bkg} comparable to the temperature of the cryogenically cooled Cu wall housed in the collision chamber. The evaporation data here are analyzed by a similar procedure; the TOF spectra are fitted by a linear combination of two MB distributions at T_{liq} (blue trace) and T_{bkg} = 131 and 123 K (cyan trace) for CD_4 and D_2O, respectively. The background contributions are significantly lower here compared to Ne evaporation.

The contributions from the two distributions are integrated at each scattering angle, resulting in the angular distributions shown in Fig. 3. The dominant contribution follows a cos θ_f distribution, as expected for an evaporation process.[64,65] Since CD_4 and D_2O evaporation follow such a distribution, along with exhibiting Maxwellian behavior, it appears that these species escape from the jet without significant distortion of angular and velocity distributions that would be expected if significant gas-phase collisions occurred post-desorption. Similar results were seen for Ne evaporation from a Ne-doped dodecane flat jet.[31] This result demonstrates that scattering experiments with CD_4 and D_2O as gas scattering partners are unlikely to be affected by beam-vapor collisions.

Regarding the isotropic contribution, the Cu cold wall temperature was experimentally measured to be 150 K. Considering the above-fitted T_{bkg} values and the lower vapor pressures of CD_4 and D_2O compared to Ne, it is reasonable that a small, constant background signal is observed as these molecules evaporate from the jet, are captured through cryo-condensation, and subsequently desorb.[66] It also follows that the isotropic background contributions for both CD_4 and D_2O are considerably smaller than those for Ne. For all three solutes, this results in a gradual spectral broadening toward

longer arrival times as θ_f increases because there is less evaporative flux from the jet owing to the cosine law. Note that for all three species, contributions such as dodecane fragments or doubly ionized residual argon background to the TOF spectra have been systematically addressed and determined not to contribute to the isotropic background.

B. Scattering

Figure 4 shows TOF spectra of Ne, CD_4, and D_2O scattered from a flat dodecane jet; as mentioned in the Introduction, Ne scattering was re-investigated here due to improved operating parameters for the quadrupole mass spectrometer. In this work, we present new data for "fast" Ne (here simply referred to as Ne and seeded in a 1:9 ratio in He), while results from "slow" Ne (pure, E_i = 6.3 kJ mol^{-1}) are reproduced from our previous work.[31] The incident angle is $\theta_i = 60°$, and results are shown at select detector angles θ_f along with TOF spectra for the incident molecular beams. Figures 5 and 6 show results in which Ne, CD_4, and D_2O molecules are scattered at incident angles of $\theta_i = 45°$ and 80°, respectively. Integrating the fitted TOF spectra for scattered Ne, CD_4, and D_2O molecules yields the angular distributions shown in Fig. 7 for the three incident angles. For all incident angles, as θ_f increases, the TOF profiles shift toward earlier arrival times, i.e., the opposite trend to what is seen in evaporation. Overall, CD_4 and D_2O scattering result in similar TOF spectra.

As in previous work, the TOF distributions are fitted using two contributions assigned to a faster component from IS and a slower one from TD. To model the IS channel during a scattering process, a flux distribution for a supersonic (SS) molecular beam was used in the fitting process,[67,68]

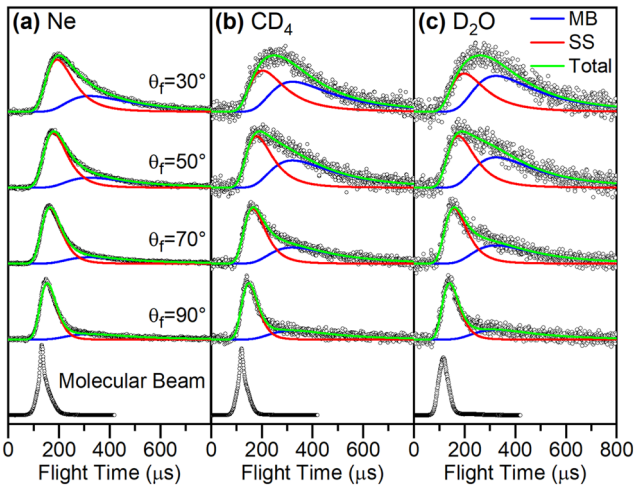

FIG. 4. Normalized TOF spectra of (a) Ne, (b) CD_4, and (c) D_2O scattering from a dodecane flat jet with $\theta_i = 60°$. The data are fitted by the sum of an SS distribution (red traces) and an MB distribution (blue traces) at the liquid jet temperature (T_{liq} = 269 K). The sum of the two contributions is shown by the green traces. The normalized temporal profiles of the pulsed molecular beams (measured without the chopper wheel) are shown at the bottom for reference. The mean translational energies E_i for Ne, CD_4, and D_2O are 23.7, 29.3, and 33.4 kJ mol^{-1}, respectively.

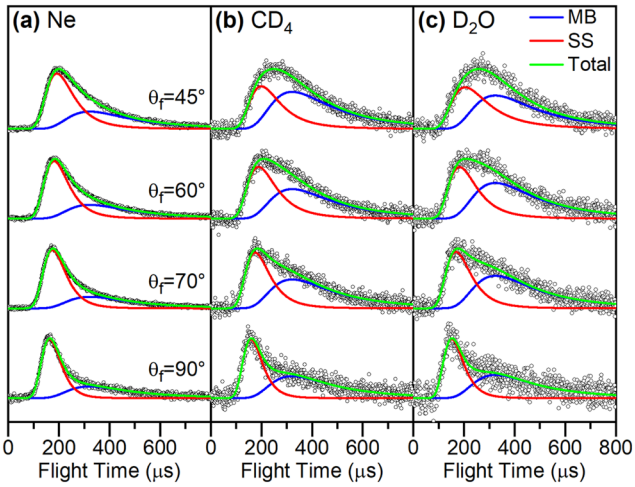

FIG. 5. Normalized TOF spectra of (a) Ne, (b) CD_4, and (c) D_2O scattering from a dodecane flat jet with $\theta_i = 45°$. The data are fitted by the sum of an SS distribution (red traces) and an MB distribution (blue traces) at the liquid jet temperature (T_{liq} = 269 K). The total fits are shown by the green traces.

$$f_{SS}(v) \propto v^3 \exp\left(-\frac{m(v - v_{SS})^2}{2RT_{SS}}\right), \tag{2}$$

with average flow velocity v_{SS} and average temperature T_{SS}. The TOF spectra are then fitted with a linear combination of SS and MB distributions representing the IS and TD scattering channels, respectively.[29,69] Note that the fitting procedure involves convolution with the molecular beam temporal profiles shown in the bottom panels of Fig. 4.

The best fit SS and MB contributions are plotted as red and blue traces, respectively, in Figs. 4–6. The general trends are that at

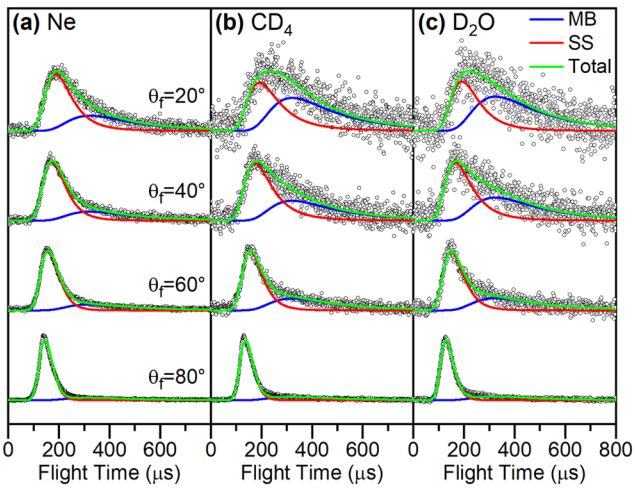

FIG. 6. Normalized TOF spectra of (a) Ne, (b) CD_4, and (c) D_2O scattering from a dodecane flat jet with $\theta_i = 80°$. The data are fitted by the sum of an SS distribution (red traces) and an MB distribution (blue traces) at the liquid jet temperature (T_{liq} = 269 K). The total fits are shown by the green traces.

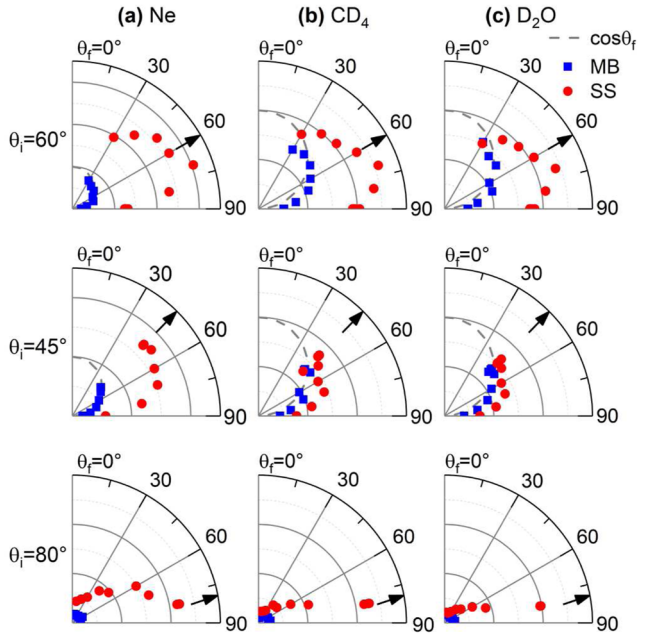

FIG. 7. Angular plots created from the integrated, non-normalized intensities of scattering with rows corresponding to θ_i = 60°, 45°, and 80° at various detector angles for columns corresponding to (a) Ne, (b) CD_4, and (c) D_2O. Blue squares represent the TD, and red circles represent the IS contributions to the TOF fits. The cosine function representing the expected angular distribution for evaporation is indicated by the dashed gray line. Arrows indicate the specular angle.

each incident angle θ_i, the relative contribution from TD decreases with increasing θ_f. This trend is consistent with the expected $\cos\theta_f$ angular distribution for TD and is the reason why the TOF distributions become narrower and faster as θ_f increases. At each θ_i, we observe that TD is considerably smaller for Ne than for CD_4 and D_2O and that the IS/TD ratios for CD_4 and D_2O are roughly equal across the entire dataset. Finally, for a given detection angle θ_f, the IS/TD ratio increases with increasing θ_i, i.e., at more grazing collisions for all three scatterers. This holds true for slow Ne scattering as well. Note that there is considerably less TD for Ne compared to our earlier work,[31] a result attributed to the improved mass spectrometer operating conditions used here. However, the same parameters in Eqs. (1) and (2) fit the TD and IS contributions to the Ne TOF spectra here and in our previous study.

Inspecting the angular dependencies of the integrated IS and TD fits for θ_i = 60° in Fig. 7, the peak intensity of the IS channel is slightly larger than the 60° specular scattering angle for all three gas scattering partners, each peaking at θ_f = 70°. This effect, which is present but less obvious at θ_i = 45°, has been observed previously in gas–solid scattering,[70,71] where it becomes more prominent as the incident beam translational energy increases. Meanwhile, the TD components follow a $\cos\theta_f$ angular distribution for all three solutes. This latter observation signifies that during scattering events, the trapped particles underwent thermal equilibration with the liquid surface. For the other two incident scattering angles, the TD components again closely follow a $\cos\theta_f$ angular distribution with IS components peaked at or near their respective specular

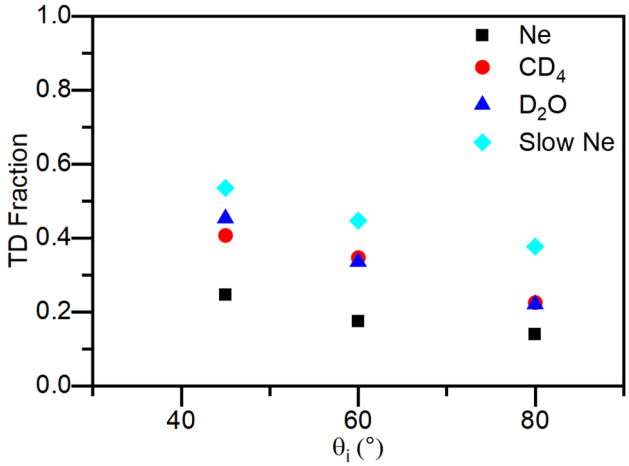

FIG. 8. TD fraction at θ_f = 60° as a function of incident angle for Ne, CD_4, D_2O, and slow Ne (E_i = 6.3 kJ mol^{-1}) scattered from a dodecane flat jet.

angles. For all three species, the increase in IS/TD ratios as both θ_i and θ_f increase has been observed previously in liquid scattering experiments.[31,33,72,73]

Figure 8 shows the TD fraction at θ_f = 60°, defined as TD/(TD + IS), for Ne, CD_4, and D_2O scattering as a function of incident angle. In addition, included are the TD fractions for slow Ne. All scatterers show that the TD fraction decreases with increasing θ_i, confirming the trend from inspection of the TOF spectra. For all three incident angles, the highest and lowest TD fractions are seen for slow and fast Ne, respectively; the TD fractions for CD_4 and D_2O are similar to one another and lie between the Ne results. This trend holds true in Fig. 9 as well, where the TD fractions for these gas scattering partners are plotted as a function of deflection angle. As χ increases, the TD fractions also increase for all three solutes.

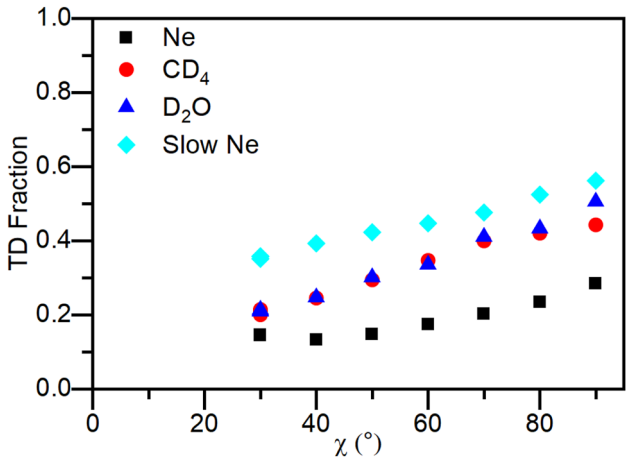

FIG. 9. TD fraction as a function of deflection angle for Ne, CD_4, D_2O, and slow Ne (E_i = 6.3 kJ mol^{-1}) scattered from a dodecane flat jet at θ_i = 60°.

C. Kinematic models

We next consider energy transfer at the interface based on the scattering experiments. Through analyzing the IS components of the TOF spectra, the change in translational energy of the incident Ne, CD_4, and D_2O beams can be deduced. As a result, the average fractional energy loss in the IS channel can be described as a function of deflection angle according to the "soft-sphere" kinematic model,[74–76]

$$\left(\frac{\Delta E}{E_i}\right) \approx \frac{2\mu}{(1+\mu)^2}\left[1+\mu(\sin\chi)^2 - \cos\chi\sqrt{1-\mu^2(\sin\chi)^2 - \frac{E_{int}}{E_i}(\mu+1)} + \frac{E_{int}}{E_i}\left(\frac{\mu+1}{2\mu}\right)\right]\left[1+\frac{V-2RT_{liq}}{E_i}\right]. \quad (3)$$

Here, the absolute change in translational energy is $\Delta E = E_i - \langle E_{IS}\rangle$, with incident translational energy E_i and average energy in the IS channel $\langle E_{IS}\rangle$. Other parameters are the mass ratio $\mu = m_{gas}/m_{eff}$ between the gas molecule and the effective surface mass (representing the mass of the surface atoms that participate in an IS event), the deflection angle $\chi = 180° - (\theta_i + \theta_f)$, the total internal excitation E_{int} (i.e., for the scatterer and the liquid), the liquid temperature T_{liq}, and the gas–surface interaction potential V. We have successfully applied this model in our Ne-dodecane scattering study, and it has found success elsewhere in other gas–liquid[76] and gas–solid[77] scattering studies.

The measured fractional translational energy loss as a function of deflection angle is plotted in Fig. 10 for Ne, CD_4, and D_2O scattering. As in previous work on liquids,[31,33,76] $\Delta E/E_i$ increases at larger values of χ and shows little or no dependence on θ_i. At $\theta_i = 60°$, the energy loss for CD_4 increases from 0.27 to 0.61 between $\chi = 30°$ and 90°. For D_2O, the analogous values vary from 0.27 to 0.64. These ranges for energy loss are similar to one another and are greater than the range of 0.15 to 0.46 observed for Ne. This trend remains true for the other two incident angles explored in this study. Numerical values for fractional energy loss at $\chi = 90°$, 60°, 45°, and 30° are listed in Table II.

With fractional energy loss plotted as a function of deflection angle, the functional form of the soft-sphere kinematic model can be fitted to the experimental data. These fits are also shown in Fig. 10. The parameters fitted are m_{eff} and E_{int}, while we estimate the gas–surface interaction potential V to be equivalent to the well depths between the scatterers and dodecane. These values are taken to be V = 0.9, 1.9, and 3.6 kJ mol^{-1} for Ne, CD_4, and

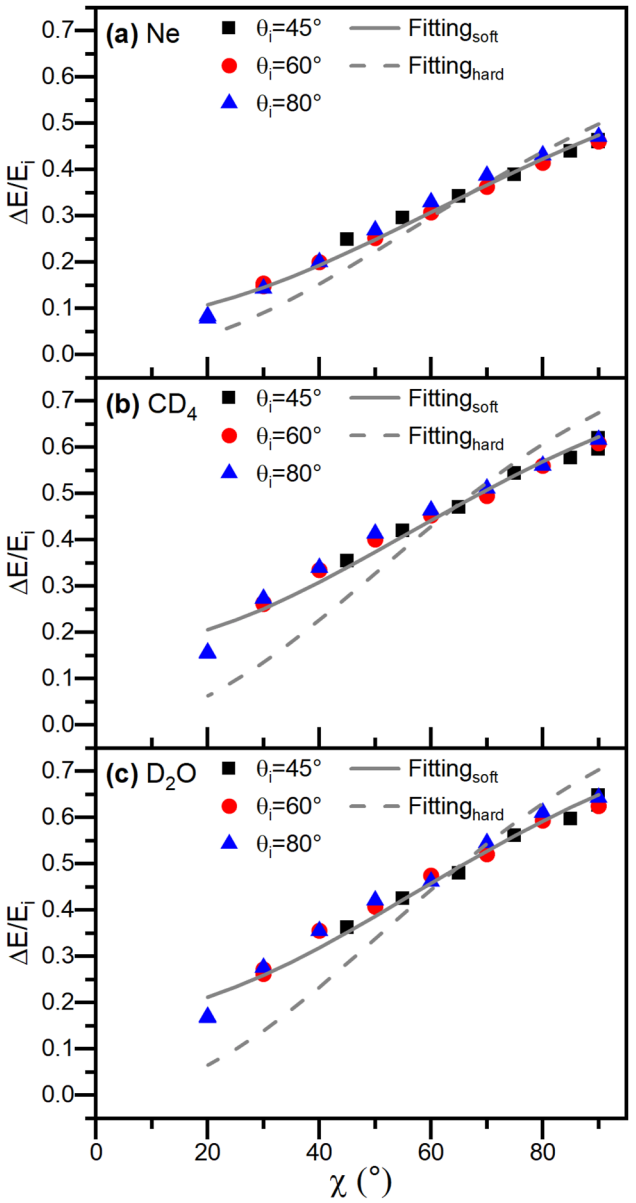

FIG. 10. Average fractional energy loss as a function of deflection angle for impulsively scattered (a) Ne, (b) CD_4, and (c) D_2O from a dodecane flat jet. Incident translational energies are 23.7, 29.3, and 33.4 kJ mol^{-1}, respectively. The solid lines give predictions for the soft-sphere model, where the incident particle interacts with a localized region of the surface with an effective mass, m_{eff}, and this region may increase its internal energy, E_{int}, during collisions. The dashed lines give predictions for the hard-sphere model where internal excitation has been set to zero. The fitting results for Ne, CD_4, and D_2O with the soft-sphere model are m_{eff} = 61, 52, and 54 amu and E_{int} = 2.1, 5.3, and 5.8 kJ mol^{-1}, respectively, whereas the hard-sphere model predicts m_{eff} = 48, 34, and 35 amu, respectively.

TABLE II. Average fractional energy loss in the IS channel at select deflection angles.

Deflection angle χ (deg)	90	60	45	30
Ne	0.46	0.32	0.25	0.15
Ne[a]	0.42	···	···	···
Ne[b]	0.58	0.43	0.36	···
CD_4	0.61	0.46	0.35	0.27
CH_4[a]	0.49	···	···	···
D_2O	0.64	0.47	0.36	0.27
D_2O[a]	0.56	···	···	···

[a]Gas scattering from liquid squalane taken from Ref. 32.
[b]Gas scattering from liquid squalane taken from Ref. 33.

D_2O, respectively.[74,78–81] Note that if V is assumed to be zero, the fitted parameters do not change substantially for any of the three scatterers.

Fitting the soft-sphere kinematic model to the fractional energy loss data results in 52 and 54 amu for the effective surface mass and E_{int} values of 5.3 and 5.8 kJ mol^{-1} for CD_4 and D_2O, respectively. As in our prior study, we found that Ne scattering from dodecane led to an effective surface mass of 61 amu with a total internal excitation of 2.1 kJ mol^{-1}. All three scatterers experience an effective surface mass less than the dodecane molecular mass, demonstrating that only part of a dodecane molecule contributes to a scattering event. In applying the soft-sphere kinematic model, it can also be seen that the energy loss in the IS channel depends only on χ rather than independently on θ_i and θ_f.

As concluded for Ne-dodecane scattering, energy transfer at the interface is reasonably well-described by a soft-sphere kinematic model for both CD_4 and D_2O scattering, although the fits are slightly poorer than for Ne. Assuming E_{int} to be zero in Eq. (3), as in the case of a "hard-sphere" kinematic model, yields much worse agreement with the fractional energy loss data for all three gas scattering partners. With recovered E_{int} values for CD_4 and D_2O scattering being larger in magnitude compared to Ne scattering, it is also observed that the hard-sphere model deviates from the soft-sphere model more strongly for these species.

IV. DISCUSSION

Key results in this work include the fractional energy loss $\Delta E/E_i$ as a function of deflection angle χ for the three scatterers, the competition between the TD and IS channels, the angular distribution seen in IS, and the extent of internal energy in the IS channel. We first consider the fractional energy loss seen in IS from dodecane, as shown in Fig. 10 and Table II. To facilitate comparison with previous experiments on squalane, Table II includes $\Delta E/E_i$ at $\chi = 90°$ from Nathanson's work for the three scatterers at the collision energies used here (interpolated from Fig. 4 in Ref. 32) and reported values by Nathanson and Minton for Ne–squalane scattering at multiple deflection angles and a collision energy of 32 kJ mol^{-1}.[33]

The key trends in Table II are that at $\chi = 90°$, the fractional energy loss in the IS channel from dodecane is smallest for Ne and highest for D_2O, in agreement with the ordering seen by Nathanson.[32] We observe that for all three scatterers, $\Delta E/E_i$ decreases at smaller values of χ. At $\chi = 45°$ and 90°, Ne exhibits a fractional energy loss of 0.25 and 0.46 in collisions with dodecane, while Nathanson and Minton found analogous values of 0.36 and 0.58 on squalane.[33] Since Ne loses less of its incident energy upon a collision with dodecane, squalane appears to be a "softer" surface than dodecane.

We next consider Figs. 8 and 9, which explore complementary aspects of the angle-dependent TD fractions. Figure 8 shows that at $\theta_f = 60°$, the TD fractions at the three incident angles $\theta_i = 45°$, 60°, and 80° exhibit the same ordering: slow Ne ($E_i = 6.3$ kJ mol^{-1}) > D_2O ≈ CD_4 > Ne. In addition, the TD fraction for all scatterers decreases with increasing θ_i. Plots at scattering angles $\theta_f = 50°$ and 70° (not shown) exhibit the same scatterer ordering and a similar dependence of the TD fraction on θ_i. Hence, more grazing collisions lead to less trapping/thermal desorption, as has also been observed in other gas–liquid scattering experiments.[31,33,72,73] This result is in contrast to gas–solid scattering studies, in which the TD fraction increases for larger angles of incidence.[82–85] This difference has been attributed to the breakdown of normal energy scaling arguments due to the increased roughness and corrugation present on liquid surfaces.[73]

Fig. 9, plotted for $\theta_i = 60°$, shows that for all three scatterers, the TD fraction drops monotonically with decreasing χ, except for a slight uptick for Ne at $\chi = 30°$. The same trend is seen for $\theta_i = 45°$ and 80° (not shown). This overall trend can be partially attributed to the $\cos\theta_f$ dependence of TD, whereby at a fixed incident angle, the TD channel is augmented as χ increases (and θ_f decreases). Since the cosine law applies to all the scatterers present in this study, identical rates of change of the TD fractions with respect to χ for each solute would be expected; however, this is not the case, as the TD fractions for Ne increase less rapidly than those for CD_4 and D_2O as χ increases. Furthermore, all scatterers under study in this work exhibit more rapid changes in TD fractions as a function of χ when compared to slow Ne from our previous work.

The relative TD fractions for the three species are consistent with Nathanson's results for squalane at $\chi = 90°$ and collision energies of about 30 kJ mol^{-1},[32] in which the TD fraction was notably higher for CD_4 and D_2O than for Ne. As was the case in squalane, the least soluble species (Ne) exhibits the lowest TD fraction (see values of K_H in Table I). However, while K_H for D_2O in dodecane is a factor of 3.5 larger than that of CD_4, the TD fractions are very close for the two species; the largest difference is at $\chi = 90°$, where the TD fractions for D_2O and CD_4 are 0.50 and 0.44, respectively. Nathanson pointed out that for squalane, a stronger correlation exists between TD fractions and free energies of solvation $\Delta G^\circ_{solv} = -RT \ln K_H$, and that appears to be the case for dodecane, too.[32] For CD_4 and D_2O, our TD fractions for dodecane at $\chi = 90°$ are about 10% smaller than those for squalane, indicating again that collisions with squalane are softer and, therefore, the surface is more likely to trap the incoming scatterers.

Examining the IS channel for $\theta_i = 60°$, we see that non-specular scattering is observed for all three gas scattering partners, in which the maximum of the IS angular distribution is shifted toward the liquid surface, i.e., super-specular behavior. This has been observed previously in the scattering of O_2 from W(110)[71] and atomic beams from Ag(111)[70] and attributed to anisotropic loss of momentum with momentum transfer favored parallel to the surface normal. Assuming energy loss from momentum transfer derived from the fitted E_{int} values occurs exclusively along the surface normal, it is expected that the IS channel intensity should peak at ~65° for Ne and 70° for CD_4 and D_2O, close to what we observe in our angular distributions. It is more challenging to discern super-specular scattering at the other two incident angles. At $\theta_i = 80°$, scattering measurements beyond $\theta_f = 80°$ are contaminated by the incident molecular beam. At $\theta_i = 45°$, the angular distributions for the IS channel are somewhat noisier, particularly for the molecular scatterers.

Fitting the data to the soft-sphere model yields E_{int} values of 2.1, 5.3, and 5.8 kJ mol^{-1} for Ne, CD_4, and D_2O, respectively. This model does not distinguish between excitation of the dodecane molecules of the liquid and internal excitation of the scatterer; the effective surface mass extracted from the soft-sphere model parameterizes the loss of incident energy but not its partitioning.[76] Given that the collision kinematics of all three scatterers are very similar (i.e., identical masses and similar collision energies), it is reasonable to assume that

the larger internal excitation for CD_4 and D_2O scattering compared to Ne scattering represents excitation of internal degrees of freedom in the molecular scatterers.

In principle, scattering can lead to the excitation of vibrational or rotational degrees of freedom. However, the lowest frequency vibrational modes for CD_4 and D_2O are the ν_4 (15.6 kJ mol^{-1}) and ν_3 (14.1 kJ mol^{-1}) bending modes,[32] respectively. Since our CD_4 and D_2O beam energies are ~30 kJ mol^{-1} with maximum fractional translational energy loss values of 60% and 65%, respectively, there is not enough overall energy available to populate these vibrational states to an appreciable degree even if one assumes no energy transfer to the liquid. Hence, we assume that the internal energies for CD_4 and D_2O scattering over and above the values obtained for Ne, 3.2 and 3.7 kJ mol^{-1}, respectively, correspond to the rotational energies of the scattered molecules. Given that rotational modes are the primary cause of differences in recovered E_{int} values between the three gases, scattered D_2O molecules are somewhat more rotationally excited than scattered CD_4 molecules. This is likely due to D_2O experiencing more torque when encountering the dodecane surface by virtue of its non-zero dipole moment. Rotational excitation is well known in solid-surface scattering to be highly dependent on the anisotropic potential between the surface and scatterer.[86,87] Similar considerations presumably hold for liquid scattering as well, which can be explored with the aid of classical trajectory calculations.[88]

V. CONCLUSIONS

In this work, we have demonstrated the first set of molecular scattering experiments from a volatile flat liquid jet with the aim of determining how additional degrees of freedom in a scatterer affect scattering and energy transfer at the gas–liquid interface. As such, we have reported results on the evaporation of CD_4 and D_2O from doped dodecane jets along with the scattering of Ne, CD_4, and D_2O from pure dodecane jets. These results have provided a fundamental understanding of the gas–liquid interface from a mechanistic standpoint, with the added benefit of recovering well-defined product angular distributions due to the incorporation of a flat liquid jet.

The evaporation TOF profiles for CD_4 and D_2O were best described by an MB flux distribution at T_{liq} after background subtraction and exhibited $\cos\theta_f$ angular distributions characteristic of evaporation from a flat surface. Through the analysis of scattering TOF and angular distributions, it was found that the scattering signal for all three scatterers could be fitted by a linear combination of a faster IS component whose angular distribution peaks at or near the specular angle and a slower TD component that exhibits a $\cos\theta_f$ angular distribution. At select incident angles for all scatterers, non-specular scattering was recovered in the IS channel and attributed to anisotropic momentum transfer at the gas–liquid interface.

It was found that Ne experienced the smallest fractional energy loss from dodecane, while D_2O experienced the largest fractional energy loss. This trend matched that from prior squalane scattering experiments.[32] Furthermore, it was observed that the fractional energy loss from dodecane was smaller than from squalane, demonstrating that squalane has a softer surface than dodecane.

Sampling various incident angles, the TD fraction was largest for collision trajectories with a larger deflection angle and smallest for grazing trajectories. CD_4 and D_2O scattering resulted in similar TD fractions, contrasting with Ne scattering. The relative TD fractions correlated best with the free energies of solvation in dodecane, consistent with the prior literature. These findings showcase the importance of collision geometry and scatterer identity in determining the likelihood of being trapped at the interface. We then applied a soft-sphere kinematic model to describe energy loss in the impulsive mechanistic channel. It was shown that both CD_4 and D_2O exhibited larger values for internal excitation than Ne, attributed to rotational excitation of the polyatomic scatterers.

We have demonstrated the feasibility of elucidating interfacial interactions by probing atomic and molecular scattering dynamics at the gas–liquid interface using a flat liquid jet. This work will serve as a useful benchmark for studying future, more volatile solvents such as water. We plan to investigate nonreactive and reactive scattering from a water flat jet in the near future, specifically with regard to concentrated saltwater solutions. These experiments are currently under way, supported by the framework provided by this study.

ACKNOWLEDGMENTS

The authors acknowledge the support provided by the Office of Basic Energy Science, Chemical Sciences Division of the U.S. Department of Energy under Contract No. DE-AC02-05CH11231. M.N.P. acknowledges additional support from the Alexander von Humboldt Foundation. The authors acknowledge Bernd Winter, Bernd Abel, and Manfred Faubel for helpful discussions in the early phases of this work.

AUTHOR DECLARATIONS

Conflict of Interest

The authors have no conflicts to disclose.

Author Contributions

Walt Yang: Conceptualization (equal); Data curation (lead); Formal analysis (lead); Investigation (lead); Methodology (equal); Software (equal); Writing – original draft (lead); Writing – review & editing (equal). **Chin Lee**: Conceptualization (equal); Data curation (equal); Formal analysis (equal); Investigation (supporting); Methodology (equal); Software (equal); Writing – review & editing (supporting). **Steven Saric**: Investigation (supporting); Writing – review & editing (supporting). **Marvin N. Pohl**: Investigation (supporting); Software (supporting); Writing – review & editing (supporting). **Daniel M. Neumark**: Conceptualization (lead); Methodology (equal); Project administration (lead); Resources (lead); Supervision (lead); Validation (lead); Writing – review & editing (equal).

DATA AVAILABILITY

The data that support the findings of this study are available from the corresponding author upon reasonable request.

REFERENCES

[1] R. M. Uppu *et al.*, Arch. Biochem. Biophys. **319**, 257 (1995).
[2] T. J. Wallington, E. W. Kaiser, and J. T. Farrell, Chem. Soc. Rev. **35**, 335 (2006).
[3] A. Singh and M. Agrawal, J. Environ. Biol. **29**, 15 (2008).

[4]R. Putikam and M.-C. Lin, Int. J. Quantum Chem. **118**, e25560 (2018).
[5]M. F. Ruiz-López *et al.*, J. Am. Chem. Soc. **141**, 16564 (2019).
[6]K. T. Valsaraj, Open J. Phys. Chem. **2**, 58 (2012).
[7]C. L. Sabine *et al.*, Science **305**, 367 (2004).
[8]B. J. Finlayson-Pitts and J. J. N. Pitts, *Chemistry of the Upper and Lower Atmosphere: Theory, Experiments, and Applications* (Academic Press, San Diego, 2000).
[9]M. G. Mason *et al.*, J. Appl. Phys. **89**, 2756 (2001).
[10]P. Jungwirth and D. J. Tobias, Chem. Rev. **106**, 1259 (2006).
[11]L. Pirondini and E. Dalcanale, Chem. Soc. Rev. **36**, 695 (2007).
[12]C. Sångeland *et al.*, Solid State Ionics **343**, 115068 (2019).
[13]M. Ahmed *et al.*, J. Phys. Chem. B **125**, 9037 (2021).
[14]Y. Li, X. Yan, and R. G. Cooks, Angew. Chem., Int. Ed. **55**, 3433 (2016).
[15]I. Nam *et al.*, Proc. Natl. Acad. Sci. U. S. A. **114**, 12396 (2017).
[16]M. E. Diveky *et al.*, J. Phys. Chem. A **125**, 3528 (2021).
[17]G. L. Richmond, Chem. Rev. **102**, 2693 (2002).
[18]J. A. McGuire and Y. R. Shen, Science **313**, 1945 (2006).
[19]P. B. Petersen and R. J. Saykally, Annu. Rev. Phys. Chem. **57**, 333 (2006).
[20]D. R. Herschbach, Faraday Discuss. **55**, 233 (1973).
[21]D. M. Neumark *et al.*, J. Chem. Phys. **82**, 3045 (1985).
[22]R. E. Continetti, B. A. Balko, and Y. T. Lee, J. Chem. Phys. **93**, 5719 (1990).
[23]W. H. Weinberg, Adv. Colloid Interface Sci. **4**, 301 (1975).
[24]J. E. Hurst *et al.*, Phys. Rev. Lett. **43**, 1175 (1979).
[25]J. A. Barker and D. J. Auerbach, Surf. Sci. Rep. **4**, 1 (1984).
[26]U. Harten *et al.*, Phys. Rev. Lett. **54**, 2619 (1985).
[27]M. J. Cardillo, Surf. Sci. **299–300**, 277 (1994).
[28]Y. Huang *et al.*, Science **290**, 111 (2000).
[29]M. E. Saecker *et al.*, Science **252**, 1421 (1991).
[30]J. A. Faust and G. M. Nathanson, Chem. Soc. Rev. **45**, 3609 (2016).
[31]C. Lee *et al.*, J. Phys. Chem. A **126**, 3373 (2022).
[32]M. E. Saecker and G. M. Nathanson, J. Chem. Phys. **99**, 7056 (1993).
[33]M. E. King *et al.*, Phys. Rev. Lett. **70**, 1026 (1993).
[34]K. C. Janda *et al.*, Surf. Sci. **130**, 395 (1983).
[35]I. Kinefuchi *et al.*, AIP Conf. Proc. **762** (2005).
[36]S. L. Lednovich and J. B. Fenn, AIChE J. **23**, 454 (1977).
[37]H. Siegbahn, J. Phys. Chem. **89**, 897 (1985).
[38]G. M. Nathanson *et al.*, J. Phys. Chem. **100**, 13007 (1996).
[39]B. Wu *et al.*, J. Phys. Chem. C **114**, 4015 (2010).
[40]S. M. Brastad and G. M. Nathanson, Phys. Chem. Chem. Phys. **13**, 8284 (2011).
[41]P. D. Lane *et al.*, J. Phys. Chem. C **124**, 16439 (2020).
[42]M. Faubel, S. Schlemmer, and J. P. Toennies, Z. Phys. D: At., Mol. Clusters **10**, 269 (1988).
[43]M. Faubel and T. Kisters, Nature **339**, 527 (1989).
[44]D. K. Lancaster *et al.*, J. Phys. Chem. Lett. **4**, 3045 (2013).
[45]M. A. Shaloski *et al.*, J. Phys. Chem. A **121**, 3708 (2017).
[46]J. R. Gord *et al.*, J. Phys. Chem. A **122**, 6593 (2018).
[47]J. A. Faust, T. B. Sobyra, and G. M. Nathanson, J. Phys. Chem. Lett. **7**, 730 (2016).
[48]T. B. Sobyra, M. P. Melvin, and G. M. Nathanson, J. Phys. Chem. C **121**, 20911 (2017).
[49]J. D. Koralek *et al.*, Nat. Commun. **9**, 1353 (2018).
[50]Y. Peng *et al.*, J. Phys. Chem. C **112**, 20340 (2008).
[51]P. J. Hesse *et al.*, J. Chem. Eng. Data **41**, 195 (1996).
[52]P. Schatzberg, J. Phys. Chem. **67**, 776 (1963).
[53]Y. T. Lee *et al.*, Rev. Sci. Instrum. **40**, 1402 (1969).
[54]Y. T. Lee, Angew. Chem., Int. Ed. Engl. **26**, 939 (1987).
[55]D. Irimia *et al.*, Rev. Sci. Instrum. **80**, 113303 (2009).
[56]C. Meng and M. H. M. Janssen, Rev. Sci. Instrum. **86**, 023110 (2015).
[57]F. T. Greene and T. A. Milne, J. Chem. Phys. **39**, 3150 (1963).
[58]M. F. Vernon *et al.*, J. Chem. Phys. **77**, 47 (1982).
[59]P. P. Radi *et al.*, J. Chem. Phys. **111**, 512 (1999).
[60]M. Ekimova *et al.*, Struct. Dyn. **2**, 054301 (2015).
[61]K. Sasse, J. Jose, and J. C. Merlin, Fluid Phase Equilib. **42**, 287 (1988).
[62]E. W. Lemmon and M. L. Huber, Energy Fuels **18**, 960 (2004).
[63]G. Comsa and R. David, Surf. Sci. Rep. **5**, 145 (1985).
[64]E. H. Kennard, *Kinetic Theory of Gases* (McGraw-Hill Book Company, New York, 1938).
[65]Z. R. Kann and J. L. Skinner, J. Chem. Phys. **144**, 154701 (2016).
[66]C. Day, *CAS—CERN Accelerator School: Vacuum in Accelerators*, edited by D. Brandt (CERN, Geneva, Switzerland, 2007), p. 241.
[67]M. D. Morse, *Atomic, Molecular, and Optical Physics: Atoms and Molecules*, edited by F. B. Dunning and R. G. Hulet (Academic Press, San Diego, CA, 1996), p. 21.
[68]A. Lebehot *et al.*, *Atomic and Molecular Beams*, edited by R. Campargue (Springer, New York, 2001), p. 237.
[69]I. Kinefuchi *et al.*, Microfluid. Nanofluid. **21**, 15 (2017).
[70]R. B. Subbarao and D. R. Miller, J. Chem. Phys. **58**, 5247 (1973).
[71]C. T. Rettner, L. A. DeLouise, and D. J. Auerbach, J. Chem. Phys. **85**, 1131 (1986).
[72]M. E. King *et al.*, J. Phys. Chem. A **101**, 6556 (1997).
[73]B. G. Perkins and D. J. Nesbitt, J. Phys. Chem. A **113**, 4613 (2009).
[74]C. T. Rettner and M. N. R. Ashfold, *Dynamics of Gas-Surface Interactions* (Royal Society of Chemistry, Cambridge, 1991).
[75]G. M. Nathanson, Annu. Rev. Phys. Chem. **55**, 231 (2004).
[76]W. A. Alexander *et al.*, Faraday Discuss. **157**, 355 (2012).
[77]N. Andric and P. Jenny, Phys. Fluids **30**, 077104 (2018).
[78]F. M. Mourits and F. H. A. Rummens, Can. J. Chem. **55**, 3007 (1977).
[79]H. A. Lorentz, Ann. Phys. **248**, 127 (1881).
[80]D. Berthelot, C. R. Hebd. Seances Acad. Sci. **126**, 1703 (1898).
[81]C.-K. Chen, M. Banaszak, and M. Radosz, J. Phys. Chem. B **102**, 2427 (1998).
[82]C. B. Mullins *et al.*, Chem. Phys. Lett. **163**, 111 (1989).
[83]C. T. Rettner *et al.*, J. Vac. Sci. Technol. A **8**, 2699 (1990).
[84]M. Head-Gordon *et al.*, J. Chem. Phys. **94**, 1516 (1991).
[85]C. T. Rettner, J. Kimman, and D. J. Auerbach, J. Chem. Phys. **94**, 734 (1991).
[86]R. B. Gerber, Chem. Rev. **87**, 29 (1987).
[87]D. C. Jacobs *et al.*, J. Chem. Phys. **91**, 3182 (1989).
[88]J. J. Nogueira *et al.*, J. Phys. Chem. A **113**, 3850 (2009).